Environmental Pollution 251 (2019) 738–745

Contents lists available at ScienceDirect

Environmental Pollution

journal homepage: www.elsevier.com/locate/envpol

The influence of humic acids on the weathering of pyrite: Electrochemical mechanism and environmental implications

Kai Zheng [a, b], Heping Li [a, *], Liping Xu [c], Shengbin Li [a], Luying Wang [a], Xiaoying Wen [a], Qingyou Liu [a, b, **]

[a] Key Laboratory of High-temperature and High-pressure Study of the Earth's Interior, Institute of Geochemistry, Chinese Academy of Sciences, Guiyang, 550081, China
[b] University of Chinese Academy of Sciences, Beijing, 100039, China
[c] Zhejiang Pharmaceutical College, Ningbo, 221116, China

ARTICLE INFO

Article history:
Received 3 November 2018
Received in revised form
11 March 2019
Accepted 12 May 2019
Available online 14 May 2019

Keywords:
Pyrite
Humic acid
Electrochemical technique
Surface analysis
Environmental implications

ABSTRACT

Pyrite weathering often occurs in nature and causes heavy metal ion pollution and acid mine drainage during the process. Humic acid (HA) is a critical natural organic material that can bind metal ions, thus affecting metal transfer and transformation. In this work, in situ electrochemical techniques combined with spectroscopic analysis were adopted to investigate the interfacial processes involved in pyrite weathering with/without HA. The results showed that the pyrite weathering mechanism with/without HA is $FeS_2 \rightarrow Fe^{2+} + 2S^0 + 2e^-$. The presence of HA did not change the pyrite weathering mechanism, but HA adsorbs on the pyrite surface and inhibits the further transformation of sulfur. Furthermore, HA and Fe(II) ions can form complex at 45.0 °C. Increased concentration of HA, decreased HA solution acidity or decreased environmental temperature would all weaken the pyrite weathering, for the above conditions cause pyrite weathering to have a larger resistance of the double layer and a larger passive film resistance. Pyrite will release 73.7 g $m^{-2} \cdot y^{-1}$ Fe^{2+} to solution at pH 4.5, and the amount decreases to 36.8 g $m^{-2} \cdot y^{-1}$ in the presence of 100 mg/L HA. This study provides an in situ electrochemical method for the assessment of pyrite weathering.

1. Introduction

Pyrite is one of the most abundant sulfide minerals in the Earth's crust. It is associated with coal and metal ore deposits, and it affects the associated minerals' geochemical processes in nature (Badrzadeh et al., 2011). As an important mineral resource, pyrite has been broadly adopted in new materials studies (Cui et al., 2017; Streltsov et al., 2017), new energy systems (Jin and Caban-Acevedo, 2015), sensors (Wang et al., 2018) and other emerging industries (Gao et al., 2017). Especially of interest, pyrite has semiconducting properties and a positive rest potential. When pyrite contacts metal or conductive minerals, galvanic interaction occurs. In the field of resources, this character is always used for leaching gold (Bas et al., 2018; Martens et al., 2018) or other conductive minerals (Han et al., 2017; Santos et al., 2016). In the environmental field, pyrite has attracted significant research interest, most commonly because pyrite can easily weather, releasing heavy metal ions following acid mine drainage (AMD) (Ferreira et al., 2016; Nieva et al., 2018; Romero-Freire et al., 2016). A region famous for its AMD environmental issues is the Iberian Pyrite Belt in southwestern Spain (Sarmiento et al., 2009; Grande et al., 2018). Generally, the AMD progress can be summarized by the following equations (Weber et al., 2004):

$$FeS_2 + 7/2O_2 + H_2O \rightarrow Fe^{2+} + 2SO_4^{2-} + 2H^+ \quad (1)$$

$$Fe^{2+} + l/4O_2 + H^+ \rightarrow Fe^{3+} + 1/2H_2O \quad (2)$$

$$Fe^{3+} + 3H_2O \rightarrow Fe(OH)_3\,(s) + 3H^+ \quad (3)$$

$$FeS_2 + 7Fe_2(SO_4)_3 + 8H_2O \rightarrow 15FeSO_4 + 8H_2SO_4 \quad (4)$$

This paper has been recommended for acceptance by Baoshan Xing.

* Corresponding author.
** Corresponding author. Key Laboratory of High-temperature and High-pressure Study of the Earth's Interior, Institute of Geochemistry, Chinese Academy of Sciences, Guiyang 550081, China.
E-mail addresses: liheping@vip.gyig.ac.cn (H. Li), liuqingyou@vip.gyig.ac.cn (Q. Liu).

https://doi.org/10.1016/j.envpol.2019.05.060
0269-7491/

Humic acids (HAs) are widely distributed in soil, water and sediment. They are often characterized by two functional groups: phenolic and carboxylic groups, and thus become the most chemically active fractions of humified natural organic matter (Loffredo and Senesi, 2008). In solution, HA can dissociate and bind metal ions (Lu et al., 2017; Zheng et al., 2018), affecting their mobility, toxicity and bioavailability (Ding, 2018a, 2018b). The HA and metal ion binding is affected by the character and electronic structure of metal ions and may produce two different complexes with a same metal ion. For instance, Pb^{2+} and HA form both bridging and unidentate complexes (Jerzykiewicz, 2004). At present, AMD and heavy metal ion pollution issues are arousing broad attention, especially with respect to sulfide mineral mines. HA has been identified as a potential efficient material to prevent these issues for its passivation and complexation characters (Sahoo et al., 2013). The metal ions (Fe^{3+}, Cu^{2+}, Pb^{2+} and Zn^{2+}) that bind to HA are ubiquitous (Gao et al., 1999). Therefore, a proper understanding of the binding of HA-metal ion complexes is highly desired. He et al. (2016) confirmed that Cu^{2+} and HA fractions could bind, and the binding characteristics were well modelled by the bi-Langmuir model. Carboxyl and phenolic groups were responsible for the Cu^{2+} sorption on the HA fractions. Yuan et al. (2018) revealed that compost-derived HAs could facilitate Fe(III) oxide reduction, and further suggested that compost-derived HAs could influence the geochemical behaviours of heavy metals, organic pollutants and nutrient elements in natural environments by facilitating the reduction of Fe(III) oxides. Xiong et al. (2018) studied the effect of adsorbed soil HA on Pb binding to goethite. The results showed that, for Pb at low levels, nearly 100% was bound as Pb bridges for HA; with increased humic substance loading, more Pb was bound to adsorbed humic substances and less to goethite.

As mentioned above, pyrite is often weathered under natural conditions and releases metal ions during this process. Meanwhile, HA may bind metal ions and thus affect metal transfer and transformation. To be sure, HA must affect pyrite weathering when both are exposed to the same near-surface oxidizing conditions, and these conditions are often present in sulfide mines. To date, when pyrite and HA were both present in a solution, the previous reports were focused on pyrite being passivated by HA (Acai et al., 2009) and the adsorption mechanism on the pyrite surface (Huang et al., 2018). Acai et al. (2009) pointed out that pyrite treatment by humic acids can be used as natural environmentally friendly method for coating mining wastes. Huang et al. (2018) confirmed that the adsorption fitted with a quasi-second order kinetic equation and was in accordance with Freundlich adsorption model. It is well-known that pyrite weathering is an electrochemical process (Rimstidt and Vaughan, 2003). However, the electrochemical progress of pyrite weathering at the presence of HA, and the HA effects on pyrite weathering remains unclear.

It is well known that HA-metal complexes are involved in electron transfer processes. In this work, pyrite weathering behaviours under different concentrations, acidities and temperatures of HA were investigated depending on in situ electrochemical techniques and Fourier transform infrared (FTIR) spectra and Raman spectral analysis. We hope to (1) reveal the pyrite weathering behaviours in HA in situ, and (2) quantitatively determine how and to what extent the HA concentration, acidity and temperature affect the pyrite weathering.

2. Experimental methods

2.1. Pyrite electrode preparation

Pyrite samples were collected from Dongchuan Pb–Zn mine (Yunnan Province, China). Reflected light microscopy and X-ray diffraction analysis indicated that the samples existed as a pure, homogeneous phase. Electron microprobe analysis confirmed that the Fe and S contents (in wt. %) of the pyrite samples are 46.89 and 52.96%, while Ni and others are 0.0015 and 0.00485%, respectively (Zheng et al., 2017). The pyrite samples were cut into an approximately cubic shape to guarantee their bottom surface, the working area, was 0.25 cm^2. Then, the samples were connected to a copper wire using silver paint on the upper surface and sealed with epoxy resin, keeping only the working surface exposed to the solution. Muñoz et al. (1998) reported this detailed electrode preparation method. Prior to each test, the mineral electrode was polished with $1200^{\#}$ carbide paper to obtain a fresh surface, degreased using alcohol, rinsed with deionized water and dried in a stream of air.

2.2. Humic acid electrolyte preparation

Humic acid (CAS 1415-93-6, Shanghai Aladdin Bio-Chem Technology Co., LTD) acts as an electrolyte. First, humic acid was dissolved in water to obtain 0.00, 10.0 and 100 mg/L solutions of electrolytes. Then, HNO_3 and NaOH solutions were used to adjust the pH of the electrolyte solutions to 2.50, 4.50 and 7.00 (Liu et al., 2018).

2.3. Electrochemical measurements

As stated previously, pyrite weathering is an electrochemical process. Therefore, its weathering character and parameters could be detected through electrochemical testing. Electrochemical measurements were performed using a computer-controlled electrochemical measurement system (PARSTAT 2273, Princeton Applied Research) with a conventional three-electrode electrolytic cell that included a platinum auxiliary electrode, a pyrite working electrode and a saturated calomel reference electrode (SCE). All other potentials in this study are quoted with respect to the SCE (0.242 V vs. standard hydrogen electrode), if not otherwise stated. To minimize the resistance of the solution between the working electrode and the reference electrode, the reference electrode was connected to a Luggin capillary.

In this work, polarization curves and electrochemical impedance spectroscopy (EIS) were used to investigate the electrochemical character of pyrite weathering. We can easily get the pyrite weathering rate depend on the polarization curve, and obtain the information about the interface, structure and the reactions taking place on the pyrite interface. The polarization curves were obtained by changing the electrode potential automatically from −250 to +250 mV (vs. open current potential, OCP) at a scan rate of 10 mV s^{-1}. The EIS tests were performed using the OCP in the frequency range of 0.001–10,000 Hz with a peak-to-peak amplitude of 10 mV. Then, the ZSimpWin 3.20 (2004) software was used to fit the impedance data. To ensure reproducibility, identical experiments were repeated at least three times (the random errors of the results of all three identical experimental were within tolerance), and all the reported results in this paper were averaged. The experiments were conducted in constant temperature baths at 25, 35 and 45 ± 1 °C.

Prior to the polarization curves and EIS tests, OCP tests were performed. During the OCP progress, the electrode potential increases for 5 min. After this, it reaches a quasi-steady state, where the steady-state is defined here as a change of less than 2 mV per 5 min. Then, the electrode was stabilized for 400 s, and the potential was recorded as the OCP. When the second and third identical experiments were performed, if the potential was not within ±5 mV (compared to the first test) when the quasi-steady state was reached, the OCP test ceased. Then, a new repeated test was performed to obtain the same OC potential as the first test when

stabilized for approximately 400 s. In this work, experimental results with variations of no more than 3% were reported.

2.4. Surface characterization measurements

The surface morphologies of corroded samples were investigated by Fourier transform infrared (FTIR) spectral analysis and Raman spectral analysis.

Five 200 mesh (~74 μm) pyrite samples were used for FTIR spectral analysis. The five pyrite samples were immersed in five different HA solutions: (1) 45.0 °C + pH 4.50 + 100 mg/L HA; (2) 35.0 °C + pH 4.50 + 100 mg/L HA; (3) 25.0 °C + pH 4.50 + 100 mg/L HA; (4) 25.0 °C + pH 2.50 + 100 mg/L HA; and (5) 25.0 °C + pH 7.00 + 100 mg/L HA. All the samples were weathered for 10 weeks and then characterized using FTIR spectra. FTIR spectra were collected on a Bruker Vertex 70 Fourier transform infrared spectrometer with an Attenuated Total Reflectance (ATR) accessory. The scanning range is 600–4000 cm^{-1} with a resolution of 4 cm^{-1} and 16 scans.

Six 1.0 cm × 1.0 cm × 0.2 cm pyrite samples were used for surface analysis. The six pyrite samples were immersed in six different solutions: (1) 45.0 °C, pH 4.50 with 100 mg/L HA, (2) 35.0 °C, pH 4.50 with 100 mg/L HA, (3) 25.0 °C, pH 4.50 with 100 mg/L HA, (4) 25.0 °C, pH 2.50 with 100 mg/L HA, (5) 25.0 °C, pH 7.00 with 100 mg/L HA and (6) 25.0 °C, pH 4.50 with 10.0 mg/L HA. After weathering for 10 weeks, the six pyrite samples were characterized using Raman spectroscopy (British Renishaw inVia Reflex type microscopic confocal laser Raman spectrometer) at a wavelength of 514 nm with a collection time of 10 s. The laser power was 50 mW to avoid the destruction of the pyrite samples.

3. Results and discussion

3.1. Polarization curves study

To estimate the environmental effect of a material, two questions must be understood. One is the stability of the material in terms of thermodynamics; another is the reaction rate in terms of kinetics. For conductive minerals, the polarization curve parameters corrosion potential (E_{corr}) and corrosion density (i_{corr}) reflect the above two factors. A more positive E_{corr} suggests that the material has a better corrosion resistance, and a larger i_{corr} reflects a faster corrosion rate of the material.

Fig. 1 shows the polarization curves of the pyrite electrode in different concentrations, different acidities and at different temperatures of humic acid solutions. The polarization curves show that the pyrite electrode showed similar polarization profiles in all conditions, suggesting the same electrochemical interaction mechanism occurs at these conditions. According to Tafel extrapolation theory (Bard and Faulkner, 2001), on a single electrode the Tafel equation can be stated as: $E = A\ln(i/i_0)$, where E is the overpotential, A is the Tafel slope, V, i is the current density, A/m^2, and i_0 is exchange current density, A/m^2. The anodic Tafel slope (b_a) is the tangent line (blue line) of Tafel curve at anode (i_a), and the cathodic Tafel slope (b_c) is the tangent line (blue line) of Tafel curve at cathode (i_c). The point of intersection of the anodic and cathodic curves is the value of E_{corr} and i_{corr}, respectively. Fig. 2 is a schematic drawing that illustrates the Tafel plot for anodic and cathodic process. The i_{corr}, E_{corr} including Tafel slopes of anode (b_a) and cathode (b_c) can observe from the polarization curves based on the extrapolation methods, and R_p, can calculate from the Stern-Geary equation $R_p = b_a b_c/[2.3\ i_{corr}\ (b_a + b_c)]$ (Koga et al., 2018). The detailed polarization results are listed in Table 1.

When electrolytes have different concentrations of HA, the experimental results showed that a higher concentration of HA caused a lower corrosion density (i_{corr}), suggesting that HA inhibits pyrite weathering by increasing the pyrite polarization resistance. When the concentration of HA was increased from 0.00 mg/L to 10.0 mg/L, the pyrite corrosion density (i_{corr}) decreased from 0.81 to 0.59 μA cm^{-2} and then decreased to 0.40 μA cm^{-2} at the HA concentration of 100 mg/L. These results mean that increasing the concentration of HA inhibits pyrite weathering, and the inhibiting efficiencies (η) were 27.2% and 50.6%. In material science, η is defined as $\eta = (i_{corr} - i^0_{corr})/i^0_{corr}$ (Solmaz et al., 2008), where i^0_{corr} and i_{corr} are the corrosion current densities when the electrolyte is without and with HA, respectively. The reaction involved in the

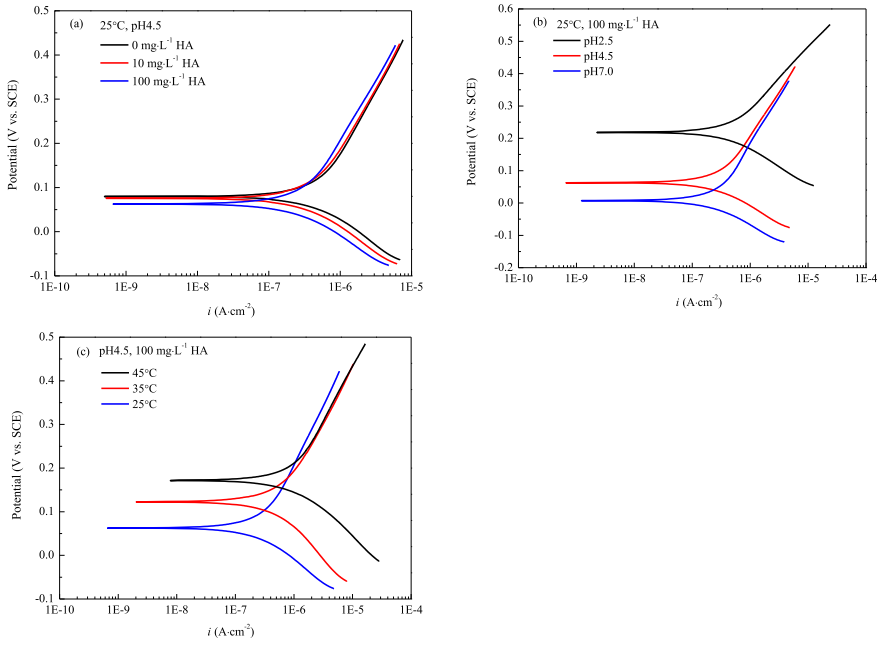

Fig. 1. Polarization curves of the pyrite electrodes in different concentrations (a), acidities (b) and temperatures (c) of HA solutions.

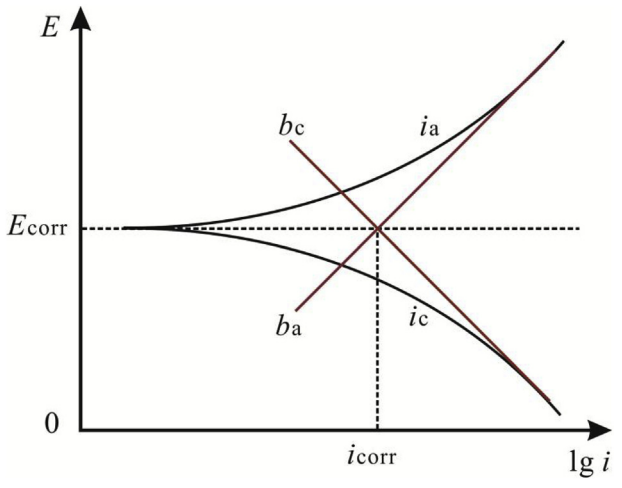

Fig. 2. Tafel slope of the anodic and cathodic process.

natural weathering of pyrite is undoubtedly an electrochemical process, and the anodic reaction is expressed as reaction (5) (Müller et al., 2014). In reaction (2), O_2 is reduced on the cathode when the electrolyte is acidic. As mentioned previously, HA has two polar functional groups, a phenolic group and a carboxylic group. HA can ionize and release H^+ and $-COO^-$ ions. A higher concentration of HA releases higher concentrations of H^+ and $-COO^-$ ions. At the cathode, the higher concentration of H^+ is favourable for O_2 reduction (Reaction (6)), and this is why the cathodic Tafel slope (b_c) is decreased. At the anode, the higher concentrations of $-COO^-$ ions favour the oxidation reaction of the complexation of $-COO^-$ and Fe^{2+} (Reaction (7)). This complexation causes the anodic Tafel slope (b_a) to decrease. It seems that the higher concentration of HA promotes pyrite electrochemical corrosion, but other facts cannot be ignored. When the complexation of $-COO^-$ and Fe^{2+} is enhanced, more S^0 is also produced. The end results from the higher concentrations of HA are that more HA and S^0 are absorbed on the electrode surface and passivate the pyrite electrode. This passivation results in an increase in the pyrite electrode polarization resistance (R_p), which causes the pyrite corrosion current density to decrease, and the pyrite weathering is weakened. The pyrite corrosion potential changed more negatively with increasing HA concentration, suggesting that pyrite easily be eroded when there is a higher concentration of HA.

The corrosion density (i_{corr}) results suggesting that higher concentration of HA inhibits the pyrite weathering, however, its corrosion potential (E_{corr}) changed more negatively, suggesting pyrite easily be eroded. These two results seem conflict but are not contradictory. From thermodynamic view, the more negatively E_{corr} reflects a bigger reaction possibility of the pyrite weathering, but not means the pyrite have faster weathering rate. From kinetic view, the smaller i_{corr} of pyrite weathering reflects a slower reaction rate, and the cause is more HA and S^0 absorbed on the electrode surface and passivate the pyrite electrode.

$$FeS_2 \rightarrow Fe^{2+} + 2S^0 + 2e^- \quad (5)$$

$$O_2 + 4H^+ + 4e^- \rightarrow 2H_2O \quad (6)$$

$$R{-}COO^{2-} + Fe^{2+} \rightarrow R{-}COOFe \quad (7)$$

When the electrolytes have different acidities, the experimental results showed that a higher pH value is a disadvantage to pyrite weathering in HA solution. When the HA solution pH changed from 2.50 to 4.50, the pyrite corrosion density (i_{corr}) decreased from 0.58 to 0.40 μA cm^{-2}, then decreased to 0.39 μA cm^{-2} at pH 7.0. The inhibiting efficiencies (η) were 31.0% and 32.8%, respectively. The causes are as follows: at the cathode, H^+ ions participate in O_2 reduction via Reaction (2). Thus, reducing the acidity (the pH changing from 2.50 to 4.50 and to 7.00) was unfavourable for O_2 reduction, and that change in acidity was why the cathodic Tafel slope (b_c) increased. At the anode, pyrite was oxidized via Reaction (1). When the HA solution pH changed from 2.50 to 4.50, the HA ionization changed more strongly, releasing more H^+ and $-COO^-$ ions. This release provoked the complexation of $-COO^-$ and Fe^{2+} ions, resulting in a polarization resistance decrease. However, the greater amount of passivated S^0 produced inhibited the pyrite anodic oxidation. This, in turn, resulted in the increase of the anodic Tafel slope (b_a).

When the electrolytes have different temperatures, the experimental results showed that a higher temperature promotes pyrite weathering in HA solution. When the temperature of HA increased from 25.0 °C to 35.0 °C, the pyrite corrosion density (i_{corr}) increased from 0.40 to 0.71 μA cm^{-2}, then increased to 1.24 μA cm^{-2} at 45.0 °C, and the promotion efficiencies (η) were 77.5% and 210%, respectively. This behaviour is explained by the fact that increasing temperature decreases the anodic and cathodic Tafel slope, and thus decreasing the polarization resistance.

3.2. Electrochemical impedance spectroscopy (EIS) study

To further understand the fundamental processes of diffusion and the faradaic reaction at the pyrite electrode, EIS studies were performed. Fig. 3(a–c) and Fig. 3 (a'-c') present the Nyquist and Bode plots, respectively, for pyrite in different concentrations, different acidities and different temperatures of humic acid solutions. The similar Bode plots revealed that they are all composed of two capacitive loops, meaning that they have the same electrochemical corrosion mechanism. The loop at high frequencies is attributed to the charge transfer resistance (R_t) corresponding to the resistance between the pyrite and the outer Helmholtz plane. The loop at low frequencies, which is slightly distorted, is related to the combination of the pseudo-capacitance impedance (because of the passive layer) and the resistance R_f. The deviation from an ideal

Table 1
Electrochemical parameters of the pyrite electrode under different concentration, acidity and temperature of HA.

Influence factors	pH	T (°C)	C_{HA} (mg/L)	E_{corr} (mV)	i_{corr} (μA·cm^{-2})	b_c (mV)	b_a (mV)	R_p (KΩ·cm^2)	η
Concentration	4.50	25.0	0.00	79.8	0.81	169	544	69.3	
	4.50	25.0	10.0	75.5	0.59	167	405	87.4	27.2%
	4.50	25.0	100	62.9	0.40	144	358	111	50.6%
Acidity	2.50	25.0	100	219	0.58	134	232	65.1	
	4.50	25.0	100	62.9	0.40	144	358	111	31.0%
	7.00	25.0	100	7.30	0.39	145	445	122	32.8%
Temperature	4.50	25.0	100	62.9	0.40	144	358	111	
	4.50	35.0	100	123	0.71	137	346	59.7	77.5%
	4.50	45.0	100	172	1.24	131	335	32.9	210%

E_{corr}: corrosion potential; i_{corr}: corrosion current density; b_a: anode Tafel slope; b_c: cathode Tafel slope; R_p: polarization resistance.

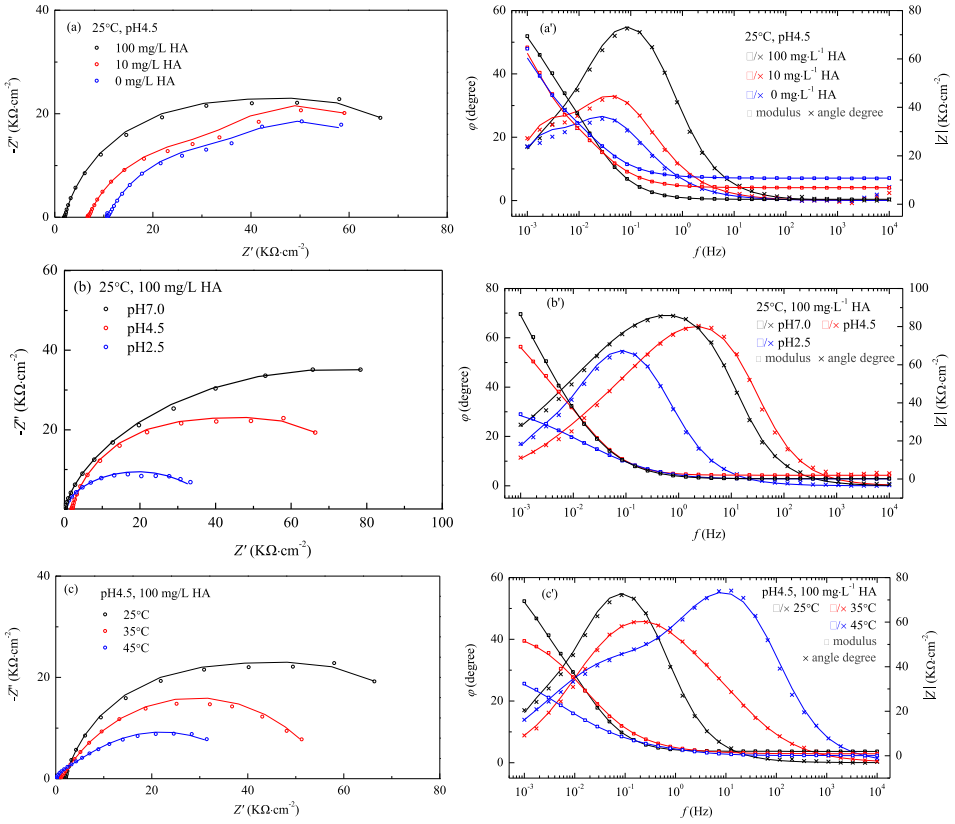

Fig. 3. Nyquist plots (a–c) and Bode plots (a'-c') for the pyrite electrodes in different concentrations, acidities and temperatures of HA solutions, where (○, □ and ×) represent the experimental values while (–) represents simulated values.

semicircle is attributed to the frequency dispersion and the inhomogeneities of the passive layer surface. The electrochemical equivalent circuit (EEC) shown in Fig. 4 was used to model the pyrite/electrolyte interface (Zheng et al., 2018). In this EEC, R_s is the ohmic resistance of the solution, R_t is the charge transfer resistance, R_f is the passive film resistance, and CPE_t and CPE_f represent the constant phase element used to replace the charge transfer capacitance at the double layer (C_t) and the passive film capacitance (C_f), respectively. The impedance of the *CPE* is given by Macdonald (1985) as:

$$Z_{CPE} = \frac{1}{Y_0(j\omega)^n} \tag{8}$$

Here, Z_{CPE} is the impedance of the constant phase element ($\Omega \cdot cm^2$), ω is the angular frequency of the AC voltage ($rad \cdot s^{-1}$), Y_0 is the magnitude of admittance of the *CPE* ($\Omega^{-1} \cdot cm^{-2} \cdot S^{-n}$), and n is a dimensionless number that defines how different the interface is from an ideal capacitor; when $n = 1$, the capacitance is considered ideal. The impedance parameters obtained by fitting the EIS data to the equivalent circuit are listed in Table 2.

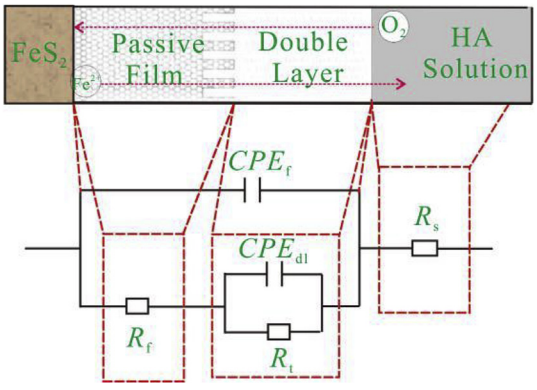

Fig. 4. Equivalent circuit for pyrite weathered in HA solution.

Comparing the pyrite electrochemical parameters in different concentrations, different acidities and different temperatures humic acid solutions, we can see that a higher concentration of HA, a higher pH value or a lower temper leads to an increase in the R_t value and a decrease in the double-layer capacitance (CPE_t, Y_0). The increase in the R_t value indicates that ions change after transport through the double-charge layer, and the decrease in CPE_t, Y_0 can be attributed to the decrease in the local dielectric constant of the electrical double layer.

The lower capacitance and the greater resistance of the double layer indicate that the increased concentration of HA, decreased HA solution acidity or decreased environmental temperature weakened the pyrite electrochemical oxidation. Furthermore, the increased concentration of HA, decreased HA solution acidity or decreased environmental temperature caused a greater passive film resistance (R_f) and a smaller passive capacitance (CPE_f, Y_0). The smaller capacitance and the greater resistance of the film on the electrode surface indicate a tighter passive film. All of these results agree with the polarization results.

3.3. Surface characterization measurements

To analyse the interaction between Fe(II) and HA particles, FTIR spectra of HA-Fe(II) were obtained and compared with the FTIR spectrum of HA. Raman spectra were used to investigate the surface products.

Table 2
Equivalent circuit model parameters for galena in electrolyte without and with 100 mg/L HA.

Influence factors	pH	T (°C)	C_{HA} (mg/L)	CPE_t, Y_0 ($S \cdot cm^{-2} \cdot s^{-n}$)	n	R_f ($\Omega \cdot cm^2$)	CPE_f, Y_0 ($S \cdot cm^{-2} \cdot s^{-n}$)	n	R_t ($\Omega \cdot cm^2$)
Concentration	4.50	25.0	0.00	3.69E-3	1.00	2.22E4	1.75E-4	0.71	4.14E4
	4.50	25.0	10.0	2.84E-3	1.00	2.86E4	1.68E-4	0.73	4.19E4
	4.50	25.0	100	1.38E-3	0.83	2.92E4	1.66E-4	0.83	5.18E4
Acidity	2.50	25.0	100	5.20E-3	0.81	6.91E3	1.82E-4	0.68	3.47E4
	4.50	25.0	100	1.38E-3	0.83	2.92E4	1.66E-4	0.83	5.18E4
	7.00	25.0	100	1.38E-4	0.87	1.68E5	6.66E-5	0.84	1.49E5
Temperature	4.50	25.0	100	1.38E-3	0.83	2.92E4	1.66E-4	0.83	5.18E4
	4.50	35.0	100	1.63E-3	0.81	5.23E3	1.72E-4	0.70	5.13E4
	4.50	45.0	100	1.78E-3	0.79	4.46E3	1.77E-4	0.53	3.78E4

R_t: charge transfer resistance; R_f: passive film resistance; n: dimensionless number; CPE_t: constant phase element of double layer; CPE_f: constant phase element of passive film.

Fig. 5 (a) shows the FTIR of the pristine pyrite. The FTIR spectroscopic data show two peaks in the region of 200–2000 cm^{-1}. The peak at 407 cm^{-1} in the FTIR spectrum corresponds to the Fe^{2+}-$[S_2]^{2-}$ stretching vibration, and the broad peak at 1081-1089 cm^{-1} might be attributed to the S–S stretching vibration of pyrite (Golsheikh et al., 2013; Rouchon et al., 2012).

Fig. 5 (b) shows the FTIR of the massive pyrite electrodes after weathering in 100 mg/L HA solutions at different acidities and temperatures. The FTIR spectroscopic data of the raw HA show that it has three different functional groups, namely, carboxyl at 1585 cm^{-1} ($-COO^-$ stretch and possibly aromatic C=C stretch), and phenol at 1385 and 1035 cm^{-1} (Baes and Bloom, 1989; Niemeyer et al., 1992). When the soaking solution contained humic acid, after pyrite weathering for 10 weeks, the FTIR spectroscopic data showed two different wavenumber bands. (1) Most FTIR spectra at the experimental conditions are similar; that is, they have 5 peaks, where three peaks (1585, 1385 and 1035 cm^{-1}) are attributed to the functional groups of HA, and two peaks (1089–1100 and 407 cm^{-1}) are attributed to the fingerprint spectrum of pyrite. The results showed that no new spectral peak occurred, meaning that pyrite (or its weathered products) and HA did not produce a chemical reaction or that its production could not be detected by FTIR at these conditions. (2) However, at the conditions of 45.0 °C and pH 4.50, in contrast to the above result, 1585 cm^{-1} for the HA carboxyl group shifted to a unresolved band at approximately 1618 cm^{-1}, possibly from the formation of HA-Fe(II) complexes. These FTIR spectra results reveal that pyrite was weathered and released Fe^{2+} ions; when Fe^{2+} ions and HA reach a high concentration at a proper pH, Fe^{2+} ions and HA can form complexes, which was also confirmed by Szilagyi (1971) and Xiong et al. (1987). However, at most conditions, Fe^{2+} ions and humic acid are difficult to complex (Gao et al., 1999).

Fig. 6 shows the Raman spectra of pristine and weathered pyrite samples. In the pristine samples, only two Raman peaks at 342 and 378 cm^{-1} were observed. The Raman peaks at 342 and 378 cm^{-1} are two of the five theoretical Raman-active modes of pyrite (Mcguire et al., 2001). After the samples were weathered in solutions with different acidities and concentrations of HA, all the Raman spectra have similar characteristic peaks, that is, except for the two pyrite characteristic peaks 342 and 378 cm^{-1}, there were another three Raman peaks at 432, 1379 and 1590 cm^{-1}. Li et al. (1992) reported the Raman peak at 432 cm^{-1} was assigned to the vibration mode of the S–S bond of elemental sulfur. In addition,

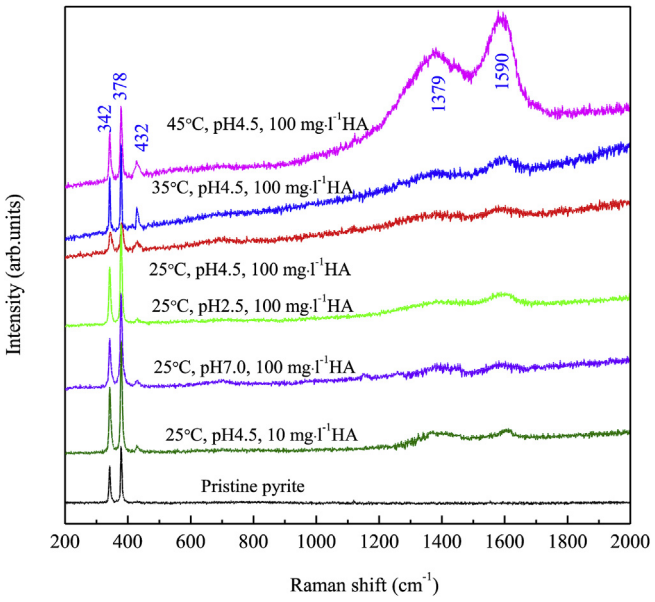

Fig. 6. Raman spectra of the pristine and weathered pyrite samples after weathering in different acidic solutions of HA.

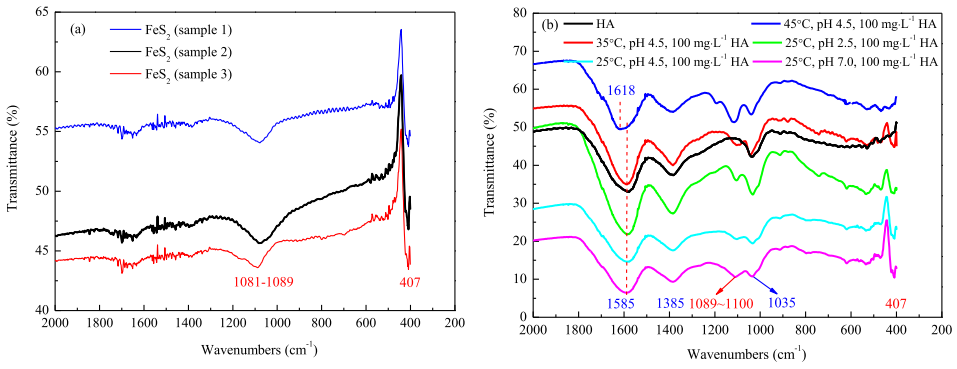

Fig. 5. FTIR spectra of the massive raw pyrite samples (a) and HA-eroded pyrite samples (b).

broad difference bands are observed at approximately 1379 cm^{-1} and 1590 cm^{-1}. These bands can be assigned to -(C–C) and -(COO^-) in the carboxylate groups of aromatic moieties and to -(C–O) of the phenols and phenolate groups of the HA structure (Roldan et al., 2011). These characteristic Raman peaks suggesting that S was formed during the pyrite weathering progress, and HA can easily adsorb on the pyrite surface. These results agree well with the above electrochemical results.

4. Electrochemical mechanism and environmental implications

As stated above, Fig. 7 shows the weathering mechanism of pyrite with and without HA via electrochemical and surface analyses. The mechanism shows that pyrite weathering releases Fe^{2+} and causes heavy metal ion pollution. HA can bind Fe^{2+} ions, and even passivate on the pyrite surface. Therefore, the environmental issues from pyrite weathering must be affected by the presence of HA.

(1) Acid mine drainage is a serious environmental issue in metal sulfide mineral mines. The accumulated H^+ ions will accelerate pyrite weathering and aggravate heavy metal ion pollution. Fig. 8 shows the pH values of pyrite pulp in various concentrations of HA solutions. The results showed, at the initial step the higher concentration of HA led to a stronger acidity, however, its acidity would change smaller ultimately. The presence of HA can inhibit pyrite weathering release of H^+ ions and thus alleviate environmental pollution in mining districts and the surrounding areas.

(2) Depending on the corrosion current density i_{corr}, we can determine pyrite weathering rate according to the Faraday equation, $v = \frac{Mi_{corr}}{nF}$ (Gunawarman et al., 2016), where v is the weathering rate, $g \cdot m^{-2} \cdot h^{-1}$, i_{corr} is the corrosion current density, $\mu A \cdot cm^{-2}$, M is the atomic weight, $g \cdot mol^{-1}$, n is the valence state, and F is the Faraday constant, 96487 C mol. For example (Table 1), in a solution at pH 4.5 without HA, the pyrite i_{corr} was 0.81 $\mu A\,cm^{-2}$, meaning that the pyrite weathering rate was 0.00842 $g\,m^{-2} \cdot h^{-1}$. That is, when the pyrite area is 1 m^2, it will release 73.7 g Fe^{2+} to the solution in a year. When solution contained 100 mg/L HA, the pyrite i_{corr} decreased to 0.40 $\mu A\,cm^{-2}$, the pyrite weathering rate was 0.00420 $g\,m^{-2} \cdot h^{-1}$, and the release of Fe^{2+} decreased to 36.8 g per year at the same conditions. Generally, higher acidity or higher alkalinity promotes pyrite corrosion, results in more serious environmental issues during pyrite weathering process. In the future, the HA, especially after modification, may be a good adsorbent to prevent these environmental issues.

(3) Temperature is an important factor affecting pyrite weathering. At 25 °C, when pyrite was in 100 mg/L pH 4.50 HA solution, its i_{corr} was 0.40 $\mu A\,cm^{-2}$, corresponding to the release of 36.8 g Fe^{2+} (1.0 m^2 area) to the solution in a year. When the environmental temperature increased to 35.0 °C, it reached 65.2 g per year at the same conditions. The natural parameters of latitude, elevation, season and others can affect the environmental temperature to considerably influence pyrite weathering.

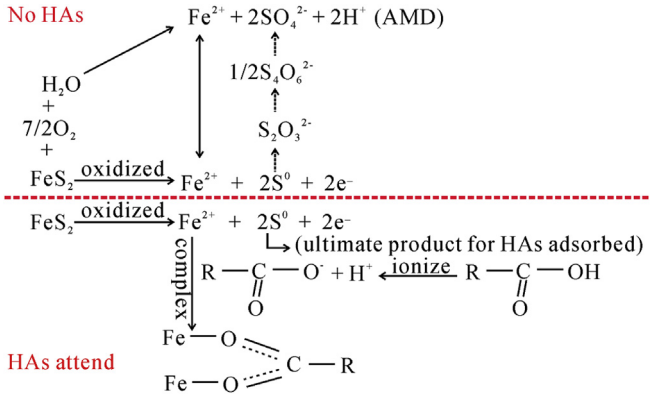

Fig. 7. The weathering mechanism of pyrite in acidic solution without/with HA.

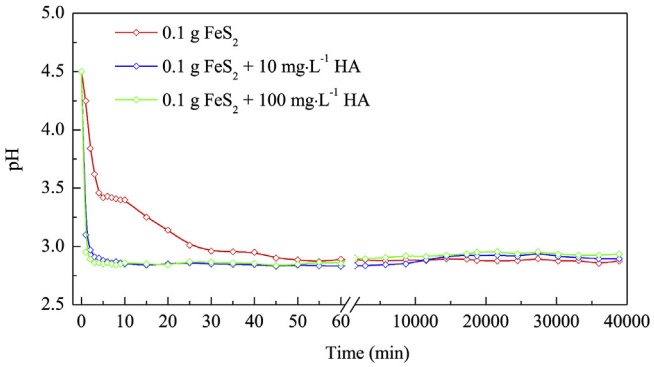

Fig. 8. The pH values of pyrite pulp in various concentrations of HA solutions.

5. Conclusions

The pyrite weathering process with/without humic acid was studied using in situ electrochemical techniques and surface analysis. The polarization curves results showed that increased concentration of HA, decreased HA solution acidity or decreased environmental temperature all weakened pyrite electrochemical oxidation, and the EIS results revealed that the above conditions cause pyrite weathering to have a lower capacitance and a larger resistance of the double layer, including a smaller passive capacitance and a larger passive film resistance. Raman spectrum revealed that the presence of HA did not change the pyrite weathering mechanism, but HA adsorbed on the pyrite surface and inhibited the further transformation of sulfur. FTIR spectra confirmed that HA and Fe(II) ions formed complexes at 45.0 °C. The Pyrite weathering mechanism with/without HA is $FeS_2 \rightarrow Fe^{2+} + 2S^0 + 2e^-$, and thus, pyrite's environmental effects with/without HA can be assessed with in situ electrochemical techniques.

Acknowledgments

This work was financially supported by the National Key R&D Program of China (Grant No. 2016YFC0600104, Large-scale Scientific Apparatus Development Program of Chinese Academy of Sciences (Grant No. YZ200720), and the “135” Program of the Institute of Geochemistry, Chinese Academy of Sciences (CAS).

Appendix A. Supplementary data

Supplementary data to this article can be found online at https://doi.org/10.1016/j.envpol.2019.05.060.

References

Acai, P., Sorrenti, E., Gorner, T., Polakovica, M., Kongolo, M., Donato, P.D., 2009. Pyrite passivation by humic acid investigated by inverse liquid chromatography.

Colloids Surf., A 337, 39–46.
Badrzadeh, Z., Barrett, T.J., Peter, J.M., Gimeno, D., Sabzehei, M., 2011. Geology, mineralogy, and sulfur isotope geochemistry of the sargaz Cu-Zn volcanogenic massive sulfide deposit, Sanandaj-Sirjan zone, Iran. Miner. Depos. 46, 905–923.
Baes, A.U., Bloom, P.R., 1989. Diffuse reflectance and transmission fourier transform infrared (DRIFT) spectroscopy of humic and fulvic acids. Soil Sci. Soc. Am. J. 53, 695–700.
Bard, A.J., Faulkner, L.R., 2001. Electrochemical Methods: Fundamentals and Applications, second ed. Wiley, New York.
Bas, A.D., Larachi, F., Laflamme, P., 2018. The effect of pyrite particle size on the electrochemical dissolution of gold during cyanidation. Hydrometallurgy 175, 367–375.
Cui, X.L., Zuo, H.E., Wen, J.K., 2017. The effect of pH on bioleaching of Deerni pyrite roasting residues as magnetic materials. Key Eng. Mater. 730, 226–230.
Ding, L.Y., Zhao, K.Y., Zhang, L.J., Liang, P., Wu, S.C., Wong, M.H., Tao, H.C., 2018a. Distribution and speciation of mercury affected by humic acid in mariculture sites at the Pearl River estuary. Environ. Pollut. 240, 623–629.
Ding, T.D., Lin, K.D., Bao, L.J., Yang, M.T., Li, J.Y., Yang, B., Gan, J., 2018b. Biouptake, toxicity and biotransformation of triclosan in diatom Cymbella sp and the influence of humic acid. Environ. Pollut. 234, 231–242.
Ferreira, V., Koricheva, J., Duarte, S., Niyogi, D.K., Guerold, F., 2016. Effects of anthropogenic heavy metal contamination on litter decomposition in streams-A meta-analysis. Environ. Pollut. 210, 261–270.
Gao, K.Z., Jack, P., Jones, J., Taylor, C., 1999. Interaction between peat, humic acid and aqueous metal ions. Environ. Geochem. Health 21, 13–26.
Gao, M.R., Zheng, Y.R., Jiang, J., Yu, S.H., 2017. Pyrite-type nanomaterials for advanced electrocatalysis. Acc. Chem. Res. 50, 2194–2204.
Golsheikh, M., Huang, N.M., Lim, H.N., Chia, C.H., Harrison, I., Muhamad, M.R., 2013. One-pot hydrothermal synthesis and characterization of FeS_2 (pyrite)/graphene nanocomposite. Chem. Eng. J. 218, 276–284.
Grande, J.A., Santisteban, M., Torre, M.L., Fortes, J.C., Miguel, E., Curiel, J., Davila, J.M., Biosca, B., 2018. The paradigm of circular mining in the world: the Iberian Pyrite Belt as a potential scenario of interaction. Environ. Earth. Sci. 77, 391.
Gunawarman, G., Refieska, A., Ilhamdi, I., Affi1, J., Cho, K., Nakai, M., Hermawan, H., Niinomi, M., 2016. Corrosion behavior of new beta type Ti-29Nb-13Ta-4.6Zr alloy in simulated body fluid solution. In: Conference: Frontiers in Bioengineering and Biotechnology, 10th World Biomaterials Congress, p. 4.
Han, B.S., Altansukh, B., Haga, K., Takasaki, Y., Shibayama, A., 2017. Leaching and kinetic study on pressure oxidation of chalcopyrite in H_2SO_4 solution and the effect of pyrite on chalcopyrite leaching. J. Sustain. Metall. 3, 528–542.
He, E., Lu, C., He, J., Zhao, B., Wang, J., Zhang, R., Ding, T., 2016. Binding characteristics of Cu^{2+} to natural humic acid fractions sequentially extracted from the lake sediments. Environ. Sci. Pollut. Res. 23, 22667–22677.
Huang, Y., Chen, H., Han, G., 2018. Research on the Adsorption of Humic Acid on Pyrite Surface. TMS Meeting & Exhibition. Springer, Cham, pp. 197–202.
Jerzykiewicz, M., 2004. Formation of new radicals in humic acids upon interaction Pb(II) ions. Geoderma 122, 305–309.
Jin, S., Caban-Acevedo, M., 2015. Solar energy conversion and electrocatalysis using earth-abundant pyrite nanomaterials. Abstr. Pap. Am. Chem. Soc. 249, 1.
Koga, G.Y., Albert, B., Roche, V., Nogueira, R.P., 2018. A comparative study of mild steel passivation embedded in Belite-Ye'elimite-Ferrite and Porland cement mortars. Electrochim. Acta 261, 66–77.
Liu, Q.Y., Li, H.P., Jin, G.H., Zheng, K., Wang, L.Y., 2018. Assessing the influence of humic acids on the weathering of galena and its environmental implications. Ecotoxicol. Environ. Saf. 158, 230–238.
Li, J.X., Zhu, X., Wadsworth, M.E., 1992. Raman spectroscopy of natural and oxidized metal sulfides. Minerals, Metals & Materials Soc Warrendale 229–244.
Loffredo, E., Senesi, N., 2008. The Role of Natural Organic Matter (Humic Substances) on Adsorption of Pesticides Possessing Endocrine Disruptor Activity. Springer, Netherlands Dordrecht, pp. 369–383.
Lu, J.H., Shi, Y.Y., Ji, Y.F., Kong, D.Y., Huang, Q.G., 2017. Transformation of triclosan by laccase catalyzed oxidation: the influence of humic acid-metal binding process. Environ. Pollut. 220, 1418–1423.
Macdonald, J.R., 1985. Generalizations of "universal dielectric response" and a general distribution-of-activation-energies model for dielectric and conducting systems. J. Appl. Phys. 58, 1971–1978.
Martens, E., Prommer, H.N., Dai, X.W., Wu, M.Z., Sun, J., Breuer, P., Fourie, A., 2018. Feasibility of electrokinetic in situ leaching of gold. Hydrometallurgy 175, 70–78.
Mcguire, M.M., Jallad, K.N., Ben-Amotz, D., Hamers, R.J., 2001. Chemical mapping of elemental sulfur on pyrite and arsenopyrite surfaces using near-infrared Raman imaging microscopy. Appl. Surf. Sci. 178, 105–115.
Müller, M., Mills, R.A., Pearce, R.B., Milton, J.A., Statham, P.J., Lloyd, J.R., Mills, M.A., Denuault, G., 2014. An electrochemical study of the influence of marinobacter aquaeolei on the alteration of hydrothermal chalcopyrite ($CuFeS_2$) and pyrite (FeS_2) under circumneutral conditions. Geomicrobiol. J. 31, 373–382.
Muñoz, J.A., Gómez, C., Ballester, A., Blázquez, M.L., González, F., Figueroa, M., 1998. Electrochemical behaviour of chalcopyrite in the presence of silver and Sulfolobus bacteria. J. App. Elechem. 28, 49–56.
Niemeyer, J., Chen, Y., Bollag, J.M., 1992. Characterization of humic acids composts and peat by diffuse reflectance fourier-transform infrared spectroscopy. Soil Sci. Soc. Am. J. 56, 135–140.
Nieva, N.E., Borgnino, L., Garcia, M.G., 2018. Long term metal release and acid generation in abandoned mine wastes containing metal-sulphides. Environ. Pollut. 242, 264–276.
Rimstidt, J.D., Vaughan, D.J., 2003. Pyrite oxidation: a state-of-the-art assessment of the reaction mechanism. Geochem. Cosmochim. Acta 67, 873–880.
Roldan, M.L., Corrado, G., Francioso, O., Sanchez-Cortes, S., 2011. Interaction of soil humic acids with herbicide paraquat analyzed by surface-enhanced Raman scattering and fluorescence spectroscopy on silver plasmonic nanoparticles. Anal. Chim. Acta 699, 87–95.
Romero-Freire, A., Fernandez, I.G., Torres, M.S., Garzon, F.J.M., Peinado, F.J.M., 2016. Long-term toxicity assessment of soils in a recovered area affected by a mining spill. Environ. Pollut. 208, 553–561.
Rouchon, V., Badet, H., Belhadj, O., Bonnerot, O., Lavédrine, B., Michard, J.G., Miska, Serge, 2012. Raman and FTIR spectroscopy applied to the conservation report of paleontological collections: identification of Raman and FTIR signatures of several iron sulfate species such as ferrinatrite and sideronatrite. J. Raman Spectrosc. 43, 1265–1274.
Sahoo, P.K., Kim, K., Equeenuddin, S.M., Michael, A.P., 2013. Current approaches for mitigating acid mine drainage. Rev. Environ. Contam. Toxicol. 226, 1–32.
Santos, E.D.L., Rivera-Santillan, R.E., Talavera-Ortega, M., Bautista, F., 2016. Catalytic and galvanic effects of pyrite on ferric leaching of sphalerite. Hydrometallurgy 163, 167–175.
Sarmiento, A.M., Nieto, J.M., Casiot, C., Elbaz-Poulichet, F., Egal, M., 2009. Inorganic arsenic speciation at river basin scales: the Tinto and Odiel rivers in the Iberian pyrite Belt, SW Spain. Environ. Pollut. 157, 1202–1209.
Solmaz, R., Kardaş, G., Yazici, B., Erbil, M., 2008. Adsorption and corrosion inhibitive properties of 2-amino-5-mercapto-1, 3, 4-thiadiazole on mild steel in hydrochloric acid media. Colloids Surf., A 312, 7–17.
Streltsov, S.S., Shorikov, A.O., Skornyakov, S.L., Poteryaev, A.I., Khomskii, D.I., 2017. Unexpected 3+ valence of iron in FeO_2, a geologically important material lying "in between" oxides and peroxides. Sci. Rep. 7, 13005.
Szilagyi, M., 1971. Reduction of Fe^{3+} ion by humic acid preparations. Soil Sci. 111, 233–235.
Wang, Y., Zhao, K.J., Tao, D.P., Zhai, F.G., Yang, H.B., Zhang, Z.Q., 2018. Application of pyrite and chalcopyrite as sensor electrode for amperometric detection and measurement of hydrogen peroxide. RSC Adv. 8, 5013–5019.
Weber, P.A., Stewart, W.A., Skinner, W.M., Weisener, C.G., Thomas, J.E., Smart, R.S.C., 2004. Geochemical effects of oxidation products and framboidal pyrite oxidation in acid mine drainage prediction techniques. Appl. Geochem. 19, 1953–1974.
Xiong, G., Zhang, H., Han, Y., 1987. Study on the nature of Fe^{3+} and Fe^{2+} bound with humic acid by Mossbauer spectroscopic method. Acta Pedol. Sin. 3, 218–225.
Xiong, J., Weng, L., Koopal, L.K., Wang, M., Shi, Z., Zheng, L., Tan, W., 2018. Effect of soil fulvic and humic acids on Pb binding to the Goethite/solution interface: ligand charge distribution modeling and speciation distribution of Pb. Environ. Sci. Technol. 52, 1348–1356.
Yuan, Y., He, X., Xi, B., Li, D., Gao, R., Tan, W., Zhang, H., Yang, C., Zhao, X., 2018. Polarity and molecular weight of compost-derived humic acid affect Fe(III) oxides reduction. Chemosphere 208, 77–83.
Zheng, K., Li, H.P., Wang, L.Y., Wen, X.Y., Liu, Q.Y., 2017. Pyrite oxidation under simulated acid rain weathering conditions. Environ. Sci. Pollut. Res. 24, 21710–21720.
Zheng, K., Li, H.P., Wang, L.Y., Wen, X.Y., Liu, Q.Y., 2018. Galena weathering under simulated acid rain conditions: electrochemical processes and environmental assessments. Environ. Sci-Proc. Imp. 20, 822–832.
Zheng, Z.Y., Zheng, Y., Tian, X.C., Yang, Z.H., Jiang, Y.X., Zhao, F., 2018. Interactions between iron mineral-humic complexes and hexavalent chromium and the corresponding bio-effects. Environ. Pollut. 241, 265–271.